International Journal of Heat and Mass Transfer 224 (2024) 125303

Contents lists available at ScienceDirect

International Journal of Heat and Mass Transfer

journal homepage: www.elsevier.com/locate/ijhmt

Machine learning-based design optimization of aperiodic multilayer coatings for enhanced solar reflection

Krutarth Khot, Prabudhya Roy Chowdhury, Xiulin Ruan *

School of Mechanical Engineering and Birck Nanotechnology Center, Purdue University, West Lafayette, IN 47906, USA

ARTICLE INFO

Keywords:
Multilayers
Radiative cooling
Genetic algorithm
Solar reflectivity

ABSTRACT

Multilayered coatings are promising and successful for applications in semiconductors, optical mirrors, and energy harvesting technologies. Amongst these, optical mirrors are essential for passive radiative cooling. Building upon the multilayer radiative cooling systems observed in snails and drawing from previous research, this study showcases the efficacy of machine learning algorithms in optimizing and gaining insights into multilayer structures. Due to the constraint of low sky window emissivity in biologically found calcite shells, focusing on solar reflectance becomes crucial to maximize the biological phenomenon found in snails. The manual search of the periodic multilayer design space for calcite with air gaps points to the maximum solar reflectance of ~89% at 170 nm layer thickness for 20 μm coating. To unlock the full potential of these multilayers, we then employ machine learning-based evolutionary optimization method - a genetic algorithm. The optimized aperiodic coating shows a significant enhancement of solar reflectance to ~99.8% for a 20 μm coating. Interestingly, the same average layer thickness of 170 nm provides maximum solar reflectance in 20 μm periodic and aperiodic calcite multilayer. Investigation of the spectral reflectance shows that layer thickness is crucial in tuning the solar reflectance. For small coatings, wavelengths with higher solar intensity are prioritized. Increasing the coating thickness allows inclusion of thicker layers to reflect longer wavelengths, leading to increasing trend of average calcite layer thickness. Further work exploring radiative cooling materials shows that calcite and barium sulfate reflect sunlight significantly better than silicon dioxide due to their refractive index contrast. Our findings and insights using bio-inspired design can provide superior solar reflectance utilizing thin coatings with modern manufacturing technology.

1. Introduction

Years of evolution in biological species have made their mechanisms a source of inspiration for driving innovation in modern technologies. Various species of plants and animals have evolved their physical and chemical constitutions to survive in different climatic conditions. *Sphincterochila boissieri* is one such snail species found in arid regions of Israel and Egypt [1,2]. These snails have adapted to survive in harsh hot and dry climates using radiative cooling with calcium carbonate (calcite - $CaCO_3$) based shells. Microscopic imaging has shown snail shells are made of layered morphological structures as shown in Fig. 1(a) adapted from Parveen et al. [3]. The underlying mechanism behind the snail's adaptation strategy can be utilized using multilayered materials to benefit modern technologies. Features of total solar reflectance can benefit radiative cooling and deep-space solar reflectors. Several of these applications have used the concept of photonic crystals in various ways to suit optical requirements.

Passive cooling in the form of daytime radiative cooling has been an important research area in the attempt to push sustainability in recent times. Li et al. have demonstrated the effectiveness of nanoparticle-based paints using $CaCO_3$ [4] and barium sulfate ($BaSO_4$) [5] for radiative cooling. These paints have shown a total solar reflectance of 95.5% and 98.1%, respectively. Peoples et al. reported that the total solar reflectance is critical for radiative cooling as every 1% of reflectance above a threshold of 85% can contribute a gain of ~10 W/m^2 of cooling power [6]. These works with nanoparticles spark curiosity about the performance and optimization of layered photonic crystals with the same base materials. As observed in snail shells, layered structures reflecting sunlight provide impetus to explore the vast design space of 1-dimensional (1-D) multilayer photonic crystals [2,3]. Researchers have studied these 1-D domains in the photonic context in recent decades

* Corresponding author.
E-mail address: ruan@purdue.edu (X. Ruan).

https://doi.org/10.1016/j.ijheatmasstransfer.2024.125303
Received 15 November 2023; Received in revised form 23 January 2024; Accepted 7 February 2024
Available online 20 February 2024

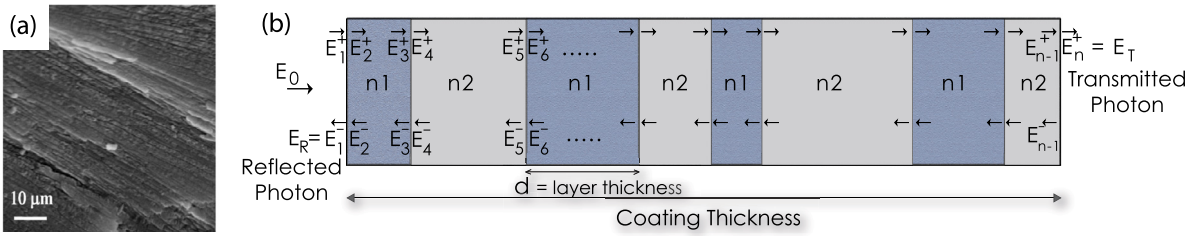

Fig. 1. (a) Layered snail shell structure made of calcite from scanning electron microscopy (SEM) image adapted from Parveen et al., 2020. For details, please refer to Ref. [3]. (b) Representation of multilayer coating with breakdown of electric field components in the multilayer, calculated using the transfer matrix formulation. Rightward moving electric field represents the transmitted component and left moving electric field represents the reflected component.

and have focused on explaining the photon localization in multilayers using the transfer matrix model [7–11]. Based on this understanding, researchers have used various intuition-based photonic crystals such as Fibonacci sequenced layer thickness structures [7,12].

An intuition-based search of a large and complex design space may often lead to solutions with sub-optimal performance and preclude exploring solutions with high performance due to unexpected physical phenomena. In contrast, machine learning(ML)-based optimization algorithms can efficiently sample much larger regions of the design space and have been shown to uncover non-intuitive solutions showing unexpected physics [13–26]. Tikhonravov et al. first demonstrated optimization for optical coatings using a genetic algorithm (GA) [27]. Due to their tunability, multilayer coatings have found numerous applications in semiconductors, energy harvesting, and optical mirror technologies over the last few decades. Attempts have been made to enhance solar cell efficiencies by using photonic crystals acting as photon reflectors and trapping mechanisms [28–31]. They have been put to use as selective emitters in photovoltaics [16,17], as thermal barrier coatings [32], and for daytime radiative cooling applications [18–24,33–37,26,25]. The radiative cooling works follow various ML-based optimization strategies focusing on selective narrow-band emission in sky window. However, considering our snail-inspired choice of calcite, which has a low emissivity in the sky window, creates an opportunity to understand and exploit the photonic reflection mechanisms prevalent in nature [38]. There exists scope for solar reflectance optimization to unlock the full potential of multilayered coatings using calcite. Additionally, it is crucial to understand and further investigate the underlying mechanisms of the reflectance enhancement through optimization for future applications.

In this work, we demonstrate the application of machine learning-based optimization to discover a novel multilayer structure that exhibits enhanced solar reflectance. The multilayer structure comprises alternating layers of the bio-inspired material- calcite, with air gaps. Our ML-based optimization method combines the rapid transfer matrix formulation with a GA optimization technique. We consider three separate evaluation functions obtained by the transfer matrix method (TMM) to optimize our bio-inspired calcite structure - total solar reflectance (R_{solar}), sky window emissivity (ε_{sky}), and the radiative cooling figure of merit (RC). These parameters are discussed in detail in Sec. 2.2.3 to Sec. 2.2.5. However, we determine reflectance optimization to be the primary focus due to the low sky window emissivity acting as a biological constraint in calcite, which is discussed further in Sec. 3.1. In this work, we hypothesize that layer thickness determines the spectral band of reflectance in these structures. To test the hypothesis, in Sec. 3.2, we conduct a manual search with varying layer thickness using a 20 μm $CaCO_3$ periodic multilayer as a benchmark and compare it with the GA-optimized aperiodic multilayer of the same total thickness. We identify that 170 nm layers provide the best solar reflectance in periodic multilayers at this total thickness; this surprisingly corresponds to the average calcite thickness in the aperiodic structure. Next, we compare this optimum periodic structure from the manual search with optimized multilayers at different total coating thickness from 5 μm to 40 μm, revealing their unlocked potential through high solar reflectance and cooling performance obtained using these non-intuitive configurations in Sec. 3.3. Using the GA and TMM framework, we optimize and further analyze similar multilayer coatings of $BaSO_4$, and SiO_2 due to their relevance to radiative cooling in Sec. 3.4. The structures studied in this work are compared to understand the effect of various design factors like layer thickness, coating thickness, refractive index and volume fraction, which can play a crucial role in the performance of multilayers. Our biologically inspired work elucidates a novel methodology for enhancing solar reflectivity using multilayer coatings that can impact radiative cooling, deep-space solar reflectors and many other crucial applications.

2. Methods

2.1. Structure and materials

We consider stacking calcite layers with air gaps, which resembles the lamellar morphology of snail shells. The stacked multilayer systems are previously modeled and studied by various research groups using a well-established transfer matrix method [8–11,28–31]. As shown in Fig. 1(b), our alternatively stacked material and air-gap multilayer system resembles a 1-D photonic crystal where we assume infinite size in the planar direction. The 1-D nature of this structure enables the use of TMM to study the photonic interaction with the multilayer. We assume all the interfaces to be ideal with no roughness for our calculations.

As discussed earlier, calcite is the primary focus of the material, chosen because of its presence in snail shell structures and abundant availability in nature. Additionally, we evaluate and compare $BaSO_4$ and SiO_2 to $CaCO_3$, as these are well known for their radiative cooling properties [5,35]. The refractive index and dielectric function for the full wavelength spectrum (~0.25 μm to ~15 μm) of $CaCO_3$ and SiO_2 have been compiled from experimental measurements and first-principles data reported in literature [38–42]. As there are no known experimental measurements for optical constants of $BaSO_4$, we use first-principles calculations data reported by Tong et al. [42]. A detailed representation of the dielectric functions can be found in the Supplementary Information (SI). The refractive index of intermediate air gaps is assumed to be 1 with no absorption and all the materials have been assumed to be non-absorbing media in the solar spectrum (0.25 μm to 3 μm).

2.2. Transfer matrix method (TMM)

We use the TMM to obtain the photon transmissivity and reflectivity in 1-D multilayers for normal incidence. The method is based on and replicates previous applications in similar morphologies performed by Ruan et al. [10,43]. This formulation provides the analytical solution to Maxwell's equations for an electromagnetic field in the 1-D system [44].

2.2.1. Analytical formulation of TMM

We consider a stratified media that reflects and transmits a uniform and normally incident electromagnetic (EM) field E_0, as shown

in Fig. 1(b). Each layer in the multilayer composed of a transmitted electric field (forward moving) and a reflected electric field (backward moving) denoted as E_j^+ and E_j^-, respectively. The transfer matrix obtains two sets of electric fields - the matrix in Eq. (1) calculates the electric field interaction at the interface and the matrix in Eq. (2) calculates the EM field between two interfaces.

$$\begin{bmatrix} E_1^+ \\ E_1^- \end{bmatrix} = \begin{bmatrix} \frac{\tilde{n_2}+\tilde{n_1}}{2\tilde{n_1}} & \frac{\tilde{n_2}-\tilde{n_1}}{2\tilde{n_1}} \\ \frac{\tilde{n_2}-\tilde{n_1}}{2\tilde{n_1}} & \frac{\tilde{n_2}+\tilde{n_1}}{2\tilde{n_1}} \end{bmatrix} \begin{bmatrix} E_2^+ \\ E_2^- \end{bmatrix} = T_{1\to2} \begin{bmatrix} E_2^+ \\ E_2^- \end{bmatrix} \tag{1}$$

$$\begin{bmatrix} E_2^+ \\ E_2^- \end{bmatrix} = \begin{bmatrix} e^{ik_{layer}d_{layer}} & 0 \\ 0 & e^{-ik_{layer}d_{layer}} \end{bmatrix} \begin{bmatrix} E_3^+ \\ E_3^- \end{bmatrix} = S_{2\to3} \begin{bmatrix} E_3^+ \\ E_3^- \end{bmatrix} \tag{2}$$

where, $k_{layer} = \frac{2\pi n_{layer}}{\lambda_0}$, refers to the wavenumber, λ_0 is the wavelength of the photon, $\tilde{n_1}$ and $\tilde{n_2}$ are the complex refractive indices of the materials given as $n+ik$, where n is the refractive index and k is the extinction coefficient, and d is the layer thickness under consideration.

We compile all the layers to get a chain of matrix multiplications, such that the transmitted electric field is given as:

$$\begin{bmatrix} E_1^+ \\ E_1^- \end{bmatrix} = T_{1\to2}S_{2\to3}T_{3\to4}...(n-layers) \begin{bmatrix} E_t \\ 0 \end{bmatrix} \tag{3}$$

where E_t is the transmitted electric field. The returning electric field gives the reflected electric field, $E_1^- = E_r$. We get the transmissivity (t) and the reflectivity (r) of the multilayer as:

$$t(\lambda) = |\frac{E_t}{E_0}|^2 \tag{4}$$

$$r(\lambda) = |\frac{E_r}{E_0}|^2 \tag{5}$$

The absorptivity (a) or emissivity (ε) is then obtained using the transmittivity and reflectivity using the relations:

$$t(\lambda) + r(\lambda) + a(\lambda) = 1 \tag{6}$$

$$a(\lambda) = \epsilon(\lambda) \tag{7}$$

2.2.2. EM field inside the multilayer

The behavior of electric field within the multilayer can be investigated by extending the TMM calculation. A layer by layer addition is performed, and electric field is evaluated whenever a layer is added. Following the previous solution approach, the electric field at any 'x' distance in the M^{th} layer at a distance x_0 from the surface can be derived as:

$$\begin{bmatrix} E_1^+ \\ E_1^- \end{bmatrix} = \prod_{i=1}^{M-1} (T_{1\to2}S_{2\to3}T_{3\to4}...) \begin{bmatrix} \frac{\tilde{n_1}+\tilde{n_2}}{2\tilde{n_2}} & \frac{\tilde{n_1}-\tilde{n_2}}{2\tilde{n_2}} \\ \frac{\tilde{n_1}-\tilde{n_2}}{2\tilde{n_2}} & \frac{\tilde{n_1}+\tilde{n_2}}{2\tilde{n_2}} \end{bmatrix} \times \begin{bmatrix} e^{ik_{layer}x_0} & 0 \\ 0 & e^{-ik_{layer}x_0} \end{bmatrix} \begin{bmatrix} E_x^+ \\ E_x^- \end{bmatrix} \tag{8}$$

The resulting local electric field is the net magnitude of both, the forward moving and the backward moving electric field and is given as:

$$|E(x)| = |E_x^+ + E_x^-| \tag{9}$$

2.2.3. Total solar reflectance

We obtain the spectral reflectance, $r(\lambda)$, from Eq. (5), which can be used as a tool to understand the underlying optical mechanisms. Furthermore, the spectral reflectance is integrated across the spectrum using a weighting function: the incident solar irradiation in the wavelength range of 0.25 μm to 3 μm on the multilayer. We use the Air Mass 1.5 (AM1.5) solar spectra by ASTM standards for our calculations [45]. This quantity is classified as the total reflectance or total solar reflectance of the coating and is calculated as:

$$R_{solar} = \frac{\int_{0.25\mu m}^{3\mu m} r(\lambda) G_{solar,AM15}(\lambda) d\lambda}{\int_{0.25\mu m}^{3\mu m} G_{solar,AM15}(\lambda) d\lambda} \tag{10}$$

where, $G_{solar,AM15}$ is the spectral solar irradiation.

2.2.4. Sky window emissivity

Sky window emissivity is essential to estimate the amount of radiation emitted by the coating into deep space within the atmospheric transmittance window of 8 μm to 13 μm. Spectral emissivity, $\varepsilon(\lambda)$, evaluated from Eq. (6) and Eq. (7) is used to calculate the sky window emissivity using weighted integration of spectral blackbody radiation at room temperature of 300 K ($I_{BB,300K}$) [46]. The ε_{sky} is defined as:

$$\epsilon_{sky} = \frac{\int_{8\mu m}^{13\mu m} \epsilon(\lambda) I_{BB,300K}(\lambda) d\lambda}{\int_{8\mu m}^{13\mu m} I_{BB,300K}(\lambda) d\lambda} \tag{11}$$

where $I_{BB,300K}$ is given as:

$$I_{BB,T}(\lambda) = \frac{2\pi hc^2}{\lambda^5} \frac{1}{e^{\frac{hc}{k_B \lambda T}} - 1} \tag{12}$$

Here, T is the temperature, h represents the Planck constant, c is the speed of light in vacuum and k_B is the Boltzmann constant.

2.2.5. Radiative cooling figure of merit

The radiative cooling figure of merit is a metric previously used to quantify the cooling capacity of various $CaCO_3$, $BaSO_4$ and hBN radiative cooling paints [4,5,47]. Considering the effects of weather conditions and locations, this parameter provides a good initial assessment for the radiative cooling in our structure. The RC is defined as:

$$RC = \epsilon_{sky} - r(1 - R_{solar}) \tag{13}$$

where r represents the ratio of solar irradiation power to the blackbody surface emissive power transmitted through the sky window. As the literature suggests, we set a standard r value of 7.14 considering ε_{sky} calculation at room temperature (300 K) [47]. This r value assumes typical peak solar irradiation and blackbody surface emissive power transmitted through sky window of 1000 W/m^2 and 140 W/m^2, respectively. Therefore, multiplying the RC-value by the blackbody surface emissive power transmitted through the sky window gives the net cooling power when the surface temperature is same as the ambient. The r-value can vary in the range of 7 to 10 depending on atmospheric conditions. We check the theoretical limit of the cooling performance using r = 7.14, which implies a case of hot and dry climate.

2.2.6. Cooling power

The heat transfer performance through radiative cooling can be evaluated by using the optical characteristics of the designed multilayers to calculate the net cooling capacity. The maximum achievable cooling power can be obtained using the following formulation used for radiative cooling applications [48,26,33]:

$$P_{cool} = P_{rad}(T_{surface}) - P_{atm}(T_{ambient}) - P_{sun} - P_{conduction+convection} \tag{14}$$

where P_{cool} is the net cooling power density. $P_{rad}(T_{surface})$ is the spectrally radiated power density at surface or sample temperature ($T_{surface}$), $P_{atm}(T_{amb})$ is the absorbed atmospheric radiation at the ambient temperature (T_{amb}), P_{sun} is the absorbed solar irradiation and $P_{conduction\ +\ convection}$ is the non-radiative heat exchange. In our work, we set the $P_{conduction\ +\ convection}$ to be 0 to focus on the radiative cooling performance. The $P_{rad}(T_{surface})$, $P_{atm}(T_{amb})$ and P_{sun} are calculated as follows:

$$P_{rad}(T_{surface}) = \int_{0.2\mu m}^{15\mu m} \epsilon(\lambda) I_{BB,T_{surface}}(\lambda) d\lambda \tag{15}$$

$$P_{atm}(T_{ambient}) = \int_{0.2\mu m}^{15\mu m} \epsilon(\lambda) \epsilon_{atm}(\lambda) I_{BB,T_{amb}}(\lambda) d\lambda \tag{16}$$

$$P_{sun} = \int_{0.2\mu m}^{3\mu m} \epsilon(\lambda) I_{AM1.5}(\lambda) d\lambda \quad (17)$$

where $I_{BB,T}$ is the blackbody radiation defined in Eq. (12), $I_{AM1.5}$ is the solar irradiation, $\varepsilon(\lambda)$ and $\varepsilon_{atm}(\lambda)$ are the spectral emissivity of the multilayer and the spectral atmospheric emissivity, respectively. The spectral emissivity, $\varepsilon(\lambda)$, is obtained using the TMM calculation.

2.2.7. Inclusion of randomness to formulate semi-coherent TMM

The transfer matrix with normal incidence assumes a coherent form for periodic multilayer structures causing constructive and destructive interference at different wavelengths. Additionally, the structure is assumed to have a perfectly smooth interface. Thus, it does not represent the results of an experimental optical measurement that can be performed for the same structure. We include an averaging step to the transfer matrix calculations to counter this phenomenon [43]. The averaging is based on incorporating transfer matrix calculations with the new thickness profiles that include randomness. A random number array is generated and normalized by its standard deviation to obtain the new thickness profile with the same average layer thickness and total thickness. The quantification is represented as follows:

$$d_i = d_0 + \delta \hat{X}_i \quad (18)$$

where, d_i refers to the layer thickness with inclusion of randomness of i^{th} layer, d_0 is the original layer thickness, δ is the user defined degree of randomness, and $\hat{X}_i$ is a normalized quantity defined using:

$$\hat{X}_i := \frac{X_i - \bar{X}}{\sigma} \quad (19)$$

where, X_i is a random number for i^{th} layer in the range of (0,1), $\bar{X}$ is the mean and σ is the standard deviation of the random number array. This strategy allows the total thickness to be fixed and the process is separately performed for the calcite layers and air gaps to maintain the prescribed volume fraction of the structure. $r(\lambda)$ and $t(\lambda)$ are evaluated using TMM for this thickness profile which is inclusive of randomness. These values are stored for all the wavelengths spanning the solar spectrum and the process is repeated for predefined iterations, each time with a unique randomness inclusive thickness profile. Finally, the $r(\lambda)$ and $t(\lambda)$ values are averaged for all the iterations, thus formulating the transfer matrix code with roughness inclusion used for the periodic 1-D multilayer.

2.3. Genetic algorithm (GA)

The design space for a multilayer system of a fixed total thickness, referred to as coating thickness in this work, is extremely large. Therefore, any intuition-based optimization is likely limited to a small region of the design space, which could easily lead to the identification of local reflectance maxima and can be a deterrent to unlocking the maximum performance. To efficiently search the entire design space and identify the global maxima, our work uses the genetic algorithm (GA). The GA is an evolutionary algorithm that tries to mimic the theory of survival of the fittest and explores the vast design space to identify and evolve strong members from the population [49]. The algorithm promotes the fitter members to the next generation and modifies them further while eliminating the weaker ones. It has been previously employed in multilayer designing for applications of x-ray reflecting mirrors and enhanced thermal conductivities, among others [13,15,27].

We discretize the multilayer structure into bits of a desired thickness to encode it in our GA. We use a bit size of 100 nm to reduce computational time for an initial comparison for R_{solar}, ε_{sky}, and RC-optimized structures. Later in this work, the bit size is reduced to 10 nm for more precise optimization. Binary indexing represents the material that makes each bit of the multilayer. A bit indexed '1' refers to the reflective material, while a bit indexed '2' refers to the air gap, with the corresponding refractive index assigned to them. The methodology works on sets of design points created within the solution space, termed 'population.' An initial population is randomly generated for the GA using the encoding system. Subsequently, it is passed through the predefined fitness function. Then the population is ranked according to their fitness values, and we perform operations on it that involve - selection, crossover, and mutation.

As the name suggests, selection is a step that selects the best-performing members of the population to proceed to the next generation. A rank-based selection process is employed in our algorithm. The top-ranked members are selected and proceed to the next generation based on a probability factor given as-

$$P(i) \propto \frac{1}{c + rank(i)} \quad (20)$$

The other members are replaced by new members formed through the crossover and mutation. Crossover helps combine different parent members of a population to generate a new member that shares attributes of the parents. We perform the single-point crossover in our GA with a probability of 0.8. It picks two parent members randomly and exchanges some part of one member with the other selected member, as shown in Fig. 2. In the final step, we perform mutation with a probability of 0.5 in randomly selected population members. This step involves interchanging randomly selected elements in the member, which helps the GA cover wider design space in search of the global maxima. Once all the operations are performed, we obtain the next generation of the population. TMM evaluates the performance of this new population and the same process is iterated further with this generation to produce the next one. We repeat it until we reach a maximum reflectance that does not vary in the following generation, indicating the global maxima of total reflectance.

3. Results and discussion

3.1. Comparison of GA optimization using R_{solar}, ε_{sky}, and RC objective functions

Our GA optimization is employed on a 20 μm calcite multilayer with three objective functions - R_{solar}, ε_{sky}, and RC. The minimum bit size for the optimization is set to 100 nm to efficiently carry out the optimization using the TMM for all the population members for the full wavelength spectrum. The R_{solar} and ε_{sky} based optimization requires 35 generations to achieve a convergence of population to the optimum of the objective function. However, due to the dependence of RC on both solar reflectance and sky window emissivity, RC-based optimization requires around 60 generations which increases the computational time.

As shown in Table 1, the maximum solar reflectance obtained from R_{solar} and RC optimization is 98.5%. The ε_{sky} also matches with a value of 0.05, which is significantly low for radiative cooling. This is expected from the dielectric function of $CaCO_3$, which shows negligible resonance in the sky window. The ε_{sky} optimization focuses solely on the maximization of $\varepsilon(\lambda)$ between 8 μm to 13 μm. Here, the best structure only converges to a sky window emissivity of 0.09; thereby, it does not demonstrate as much benefit as expected or required. This is a constraint offered by nature itself which evolved using these $CaCO_3$ shells with low sky window emissivity. The spectral reflectivity and emissivity of all three multilayers can be found in the SI. A comparison of the RC in these structures reveals both R_{solar} and RC-optimized multilayers have equal RC of -0.06, while ε_{sky} optimized structure shows an RC of -1.17. These RC values are much smaller compared to calcite-based nanoparticle white paint developed by Li et al., which shows an RC of 0.49 [4]. Although, in their case, the paint thickness is larger and much of the sky window emissivity is contributed by the acrylic matrix of the paint.

The resulting volume fractions of the three structures indicate the underlying optimization mechanisms. To maximize R_{solar} increasing the

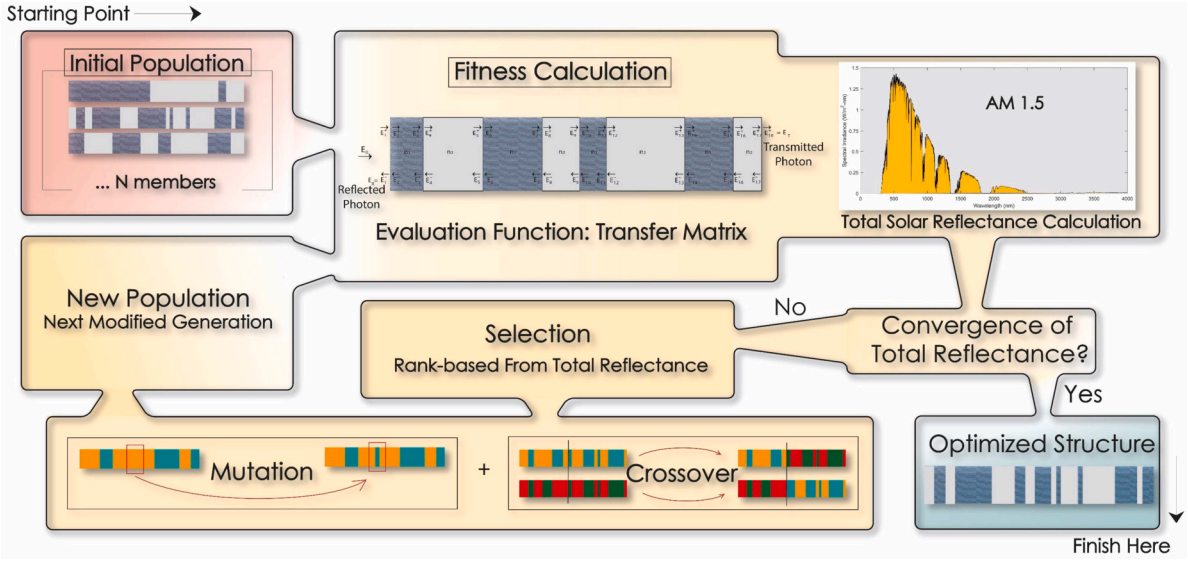

Fig. 2. The genetic algorithm (GA) optimization methodology workflow shows the various steps taken to explore design space and to obtain the optimized multilayer structure. Starting with an initial population, the fitness is obtained using total reflectance as one example of the objective function. If the maximum total reflectance does not converge, the GA evolves the population using selection, crossover, and mutation. The process is iterated until the optimized structure is obtained, as shown in the green box. (For interpretation of the colors in the figure(s), the reader is referred to the web version of this article.)

Table 1
Optimization results using R_{solar}, ε_{sky}, and RC as objective functions respectively.

Objective Function \ Result	R_{solar}	ε_{sky}	RC	Calcite Volume Fraction
R_{solar}	0.985	0.05	-0.06	0.48
ε_{sky}	0.823	0.09	-1.17	0.75
RC	0.985	0.05	-0.06	0.52

number of interfaces can enhance localization discussed later in this work. The logic aligns with RC optimization, as solar reflectance has a greater influence on RC. However, the GA moves towards structures with more calcite since air gaps cannot provide emissivity, which compromises R_{solar}.

Furthermore, we choose to use R_{solar} as the objective function in the following sections of this work because of three main reasons - similarity in results from R_{solar} and RC optimization, the negligible influence of ε_{sky} on RC and significant reduction of computation. As discussed earlier, the R_{solar} and RC optimized structures converge to the same maximum. This is a consequence of the nearly zero absorption of the biologically present calcite in the sky window range, which makes solar reflectance the lead contributor to radiative cooling. Using the full spectrum also scales up the computations as TMM calculates spectral reflectance, transmittance and emission for all wavelengths and for all members of each iterated population. Subsequently, the choice of only using the solar spectrum is justified as it can reduce computations and enable a more precise search using a smaller bit size for the GA encoding.

3.2. Manual search for periodic design and GA optimization of 20 μm calcite multilayer

We manually search for enhancement of total solar reflection by considering a periodic photonic crystal multilayer with a coating thickness of 20 μm using calcite as our reflective material. The layer thicknesses are varied from 100 nm to 500 nm with up to ±15% randomness to study the reflectance performance for periodic multilayers in TMM. We analyze the spectral reflectance of 100 nm, 200 nm and 300 nm layer structures since they show higher solar reflectance, as shown in Fig. 3(a). Reflectance peaks are observed depending on the layer thickness due to the opening up of a photonic bandgap [11,50]. Fig. 3(a) shows one broad spectral reflectance band corresponding to each structure. The 100 nm layer structure reflectance band lies in 200-800 nm range; for 200 nm layer structure, this reflectance band shifts to the 900-1400 nm range. For the 300 nm layers, it lies in the 1500-1900 nm range. Roughly, photons with a wavelength ~5-6 times the layer thickness are localized in our periodic multilayer structures of $CaCO_3$. As we increase the layer thickness, the reflectance peaks shift towards longer wavelengths. This shifting can be accounted to the shifting of the photonic band gap. The wavelength range of this band is consequential for reflecting the solar spectrum as it should correspond to peak solar irradiation.

We maximize the solar reflectance by GA optimization on the 20 μm calcite multilayer using 10 nm bits for encoding. The GA population evolves with each passing generation leading to the maximum reflectance, as shown in Fig. 3(b). The GA optimized structure of 20 μm thickness shows a total reflectance of 99.8%. This structure has 111 mixed large and small layers with calcite as the first and last layer of the multilayer structure. The average calcite layer thickness is 171 nm and the air gap is 189 nm. The volume fraction of calcite in the optimized multilayer, thus, accounts to 0.47, which is similar to the periodic multilayer volume fraction of 0.5.

We further analyze the layer thickness dependence of the periodic and optimized aperiodic structures. Both indicate high reflectance in the 150 nm to 200 nm average layer thickness range, as shown in Fig. 3(c). In periodic structures, we observe that the coatings with ~150-200 nm layers have their spectral high-reflectance bands coinciding with the peak of solar irradiation, maximizing the solar reflectance. The GA traverses the vast design space with smaller and larger average layer thicknesses. Population evolution leads the design space to an average calcite layer thickness of 150 nm to 200 nm. This broadly agrees with our findings that the total reflectance depends on the average layer thickness. We observe the maximum solar reflectance for the periodic

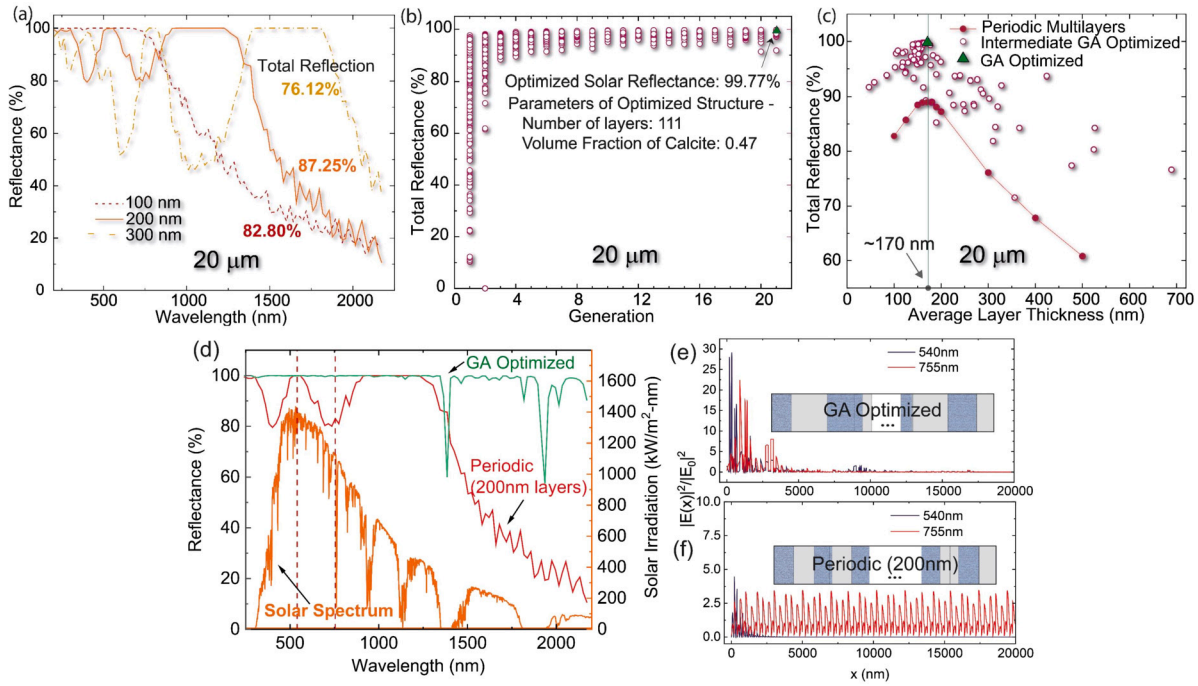

Fig. 3. (a) Spectral reflectance and total reflectance for periodic multilayers using layer thicknesses from manual search with inclusion of randomness up to ±15%. (b) Evolution of 20 μm multilayer structures during the GA optimization shows the progression to the optimized structure composed of 111 layers and 0.47 volume fraction calcite. (c) Comparison of total reflectance for manual search using different layer thicknesses of periodic multilayers and GA optimization for 20 μm coating. (d) Spectral reflectance comparison of GA optimized coating and periodic multilayer coating of 200 nm layers with reference to solar irradiation spectrum. Dotted lines mark the 540 nm and 755 nm wavelengths used for electric field analysis. (e) Electric field intensity inside the GA-optimized coating shows localization at $\lambda =$ 540 nm and $\lambda = 755$ nm. (f) Electric field propagation inside the periodic multilayer of 200 nm layers, showing localization at $\lambda = 540$ nm and no localization at $\lambda = 755$ nm.

coating of 88.98% at a layer thickness of 170 nm. Interestingly, the average calcite layer thickness for maximum reflectance coincides for the manually searched periodic multilayer and GA-optimized aperiodic multilayer.

We investigate further by comparing the spectral reflectance of the periodic structure of 200 nm layers and the GA optimized structure in Fig. 3(d). Using the AM1.5 solar spectrum for reference, the optimized design shows near 100% reflectance at wavelengths corresponding to higher solar irradiation. However, the periodic structure shows dips in reflectance at different wavelengths. This makes the optimized system better performing compared to the periodic multilayer. We also calculate the electric field intensity within the coatings to elucidate the effect of photon localization. The electric field is plotted at any distance 'x' inside the multilayer coating for the GA optimized and the periodic structure in Fig. 3(e) and Fig. 3(f), respectively. We consider wavelengths of $\lambda =$ 540 nm and $\lambda =$ 755 nm as sampling points marked with dotted lines in Fig. 3(d), as the intensity of solar irradiation is considerably high in those wavelengths. The electric field amplitude in the GA-optimized coating shows a robust localization at the beginning, with the field magnitude much greater than the incident E_0 at both wavelengths. The periodic coating localizes 540 nm wavelength reasonably; as a result, it provides near 100% reflectance for these photons. However, the extent of localization for this periodic structure is low for the wavelength of 755 nm, as demonstrated by the oscillating electric field. The oscillating electric field implies propagating EM waves in the multilayer resulting in the transmission of these photons, thereby reducing the solar reflectance at that wavelength. On the other hand, the localization demonstrated by the optimized structure leads to the decay and attenuation of the EM waves leading to opaque properties desirable in the multilayer. The GA improves upon the shortcomings of the periodic structure by including layers of various thicknesses in the multilayer. The layer thickness distribution helps the multilayer coating to localize photons at wavelengths that are not localized in the periodic structure.

3.3. Optimization of calcite multilayers for different total thicknesses

Next, GA optimization is performed for 5 μm, 10 μm, 20 μm and 40 μm coating thickness. The optimized total reflectance is compared with a baseline periodic structure of 0.5 volume fraction calcite and 170 nm layers derived from the 20 μm multilayer manual search. The GA-optimized designs show superior and unmatched total reflectance compared to the baseline structures, as shown in Fig. 4(a). We observe the total reflectance values increase as the total thickness increases and eventually starts plateauing. The trend of increasing reflectance with increasing coating thickness and saturation at higher thickness is a known artifact in multilayers.

We evaluate the cooling capacity of the optimized aperiodic multilayers to quantify the cooling performance. Figure 4(b) shows the spectrally radiated power density (P_{rad}) and net cooling power density (P_{cool}) for the optimized multilayers calculated using the heat transfer formulation described in Sec. 2.2.6. To estimate the cooling power, the ambient atmospheric temperature (T_{amb}) is set to 300 K (27 °C). We consider three hypothetical cases of temperature differential between the surface (T_s) and the ambient as - case I) $T_s = 310$ K, case II) $T_s = 300$ K which is the neutral case, and case III) $T_s = 290$ K. As expected, the net cooling power increases as thickness increases owing to the increased solar reflectance and emissivity. In the neutral scenario of no temperature differential (case II), the 40 μm optimized multilayer delivers the best cooling performance (P_{cool}) of 53 W/m^2 and the highest P_{rad} of 145.78 W/m^2. P_{cool} and P_{rad} increase in case I as higher surface temperature contributes to higher emissive power. In case III, P_{cool} and P_{rad} drop but are still net positive which demonstrates sub-ambient cooling due to the $CaCO_3$ multilayers. In addition, we also calculate the radiative cooling figure of merit for these structures, as shown in Fig. 4(c). The RC figure of merit is a unitless parameter used to evaluate radiative cooling performance using a special case of the cooling power calculation ($T_s = T_{amb}$). The RC-value is negative for smaller thickness as both

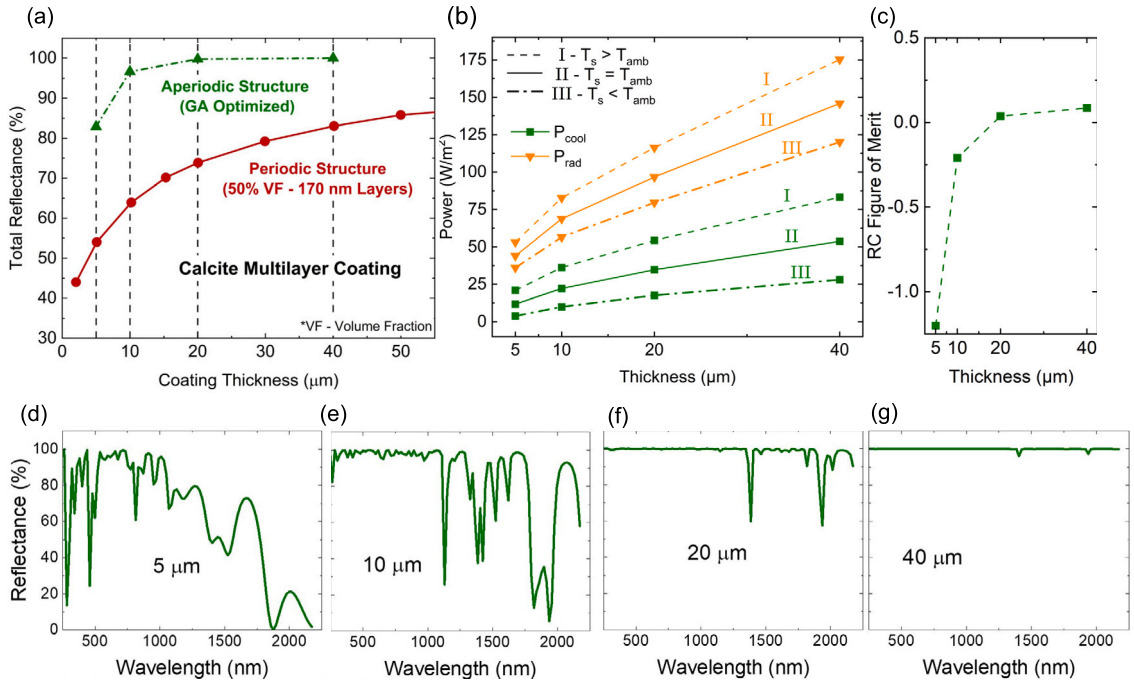

Fig. 4. (a) Comparison of optimized total reflectance for different coating thicknesses with best periodic multilayers of 170 nm calcite layer thickness (from optimum of manual search results in Fig. 3). (b) Spectrally emitted power density (P_{rad}) and net cooling power density (P_{cool}) of optimized calcite aperiodic multilayers at different thicknesses calculated for three cases of surface temperature (T_s) and ambient temperature (T_{amb}) - (I) $T_s > T_{amb}$, (II) $T_s = T_{amb}$, and (III) $T_s < T_{amb}$ using temperature differential of 10 K. (c) Radiative cooling figure of merit of optimized calcite aperiodic multilayers at different thicknesses. Spectral reflectance of optimized coating of (d) 5 μm, (e) 10 μm, (f) 20 μm, and (g) 40 μm total thicknesses.

the solar reflectivity and sky window emissivity are low. As the thickness increases, the figure of merit also indicates sub-ambient cooling.

Further insights into the optimization are obtained by analyzing the spectral reflectance of the optimized structures, as shown in Fig. 4(d)-(g). The spectral response manifests the prioritization of reflectance in the wavelength region of high solar irradiation intensity (~400 to 1000 nm). This prioritization is distinctly visible in a small coating thickness of 5 μm and to an extent, in 10 μm. GA makes this possible by stacking up layers of appropriate smaller and larger thicknesses to localize photons across the solar spectrum. Due to the small total thickness, GA can only stack up layers that can help reflect the high-intensity part, which are comparatively shorter wavelengths of solar irradiation. As we increase the coating thickness to 20 μm, GA acquires more flexibility to localize the longer wavelengths of the solar spectrum as well. It can do so by including layers of larger thickness in the multilayer structure. We observe that thicker layers are essential to localize longer wavelengths of photons, thus enhancing the solar reflectance of the coating. The layer thickness distribution of the optimized multilayer structures can be found in Fig. S3 of the SI. A crucial attribute obtained in the analysis shows that the volume fraction of calcite in these GA-optimized structures is ~0.5 in all four cases.

3.4. Comparison of GA optimization for $CaCO_3$, $BaSO_4$ and SiO_2 multilayers

Furthermore, we analyze the trends in total solar reflectance, average layer thickness, and volume fraction with increasing total thickness for optimized multilayers obtained from the GA for $CaCO_3$. We repeat the same study for $BaSO_4$ and SiO_2 to establish and concretize a correlation. The trends obtained from GA optimization have been compiled in Fig. 5. Figure 5(a) compares the total reflectance for the three materials. $CaCO_3$ gives the best performance, followed by $BaSO_4$, then SiO_2. As expected from previous studies, the refractive index contrast plays a role in determining the overall performance of total reflectance [8–10]. $CaCO_3$ and $BaSO_4$ show nearly similar total reflectance, while SiO_2 has a smaller refractive index contrast with air, as shown in Fig. 5(c), provides a smaller total reflectance. The comparison of average material layer thickness GA optimized structures at a fixed total thickness in Fig. 5(b) agrees with our prior investigation using calcite. The interesting finding obtained here is on the volume fraction. We map out the shaded areas for each material in Fig. 5(d). In all the cases we considered for optimization, the volume fraction obtained is in the 40 to 50% range. However, we note the exception for optimization at 40 μm, where the volume fraction is slightly >50% in all three cases. We believe this is because of the saturation of total reflectance to >99.9% obtained due to the large thickness of the coating. The average thickness of air gaps in Fig. 5(e) does not show an increasing trend, however, it shows a consistent range between 150 nm to 200 nm.

These results indicate that layer thickness is crucial for multilayer designs offering photonic reflection. The choice of layer thickness affects the opening up of the photonic band gap in the periodic structures and localization of photons in aperiodic (optimized) structures, thus, determining the wavelength band where reflectance is observed [11]. The photonic band gaps generate evanescent waves in that spectrum, decaying exponentially through the multilayer. This localization of photons leads to the maximization of solar reflectance in multilayered systems. The underlying phenomenon observed here can be used to determine the layer thickness in multilayer mirror design for various applications. This machine learning-based optimization using GA exploits the photon localization behavior to optimize the layer thicknesses such that wavelengths across the solar spectrum can be effectively reflected. However, the longer wavelengths observe a small coating thickness as a single homogeneous dielectric and hence, do not get localized within it. To compete with them, the GA accommodates some larger and smaller layers to create localization across the spectrum which is only possible when the coating thickness increases. As a result, we obtain a total solar reflectance of 99.8% at 20 μm coating thickness with calcite, which is the main constituent and most important player for a snail's shell to survive in hot and dry conditions.

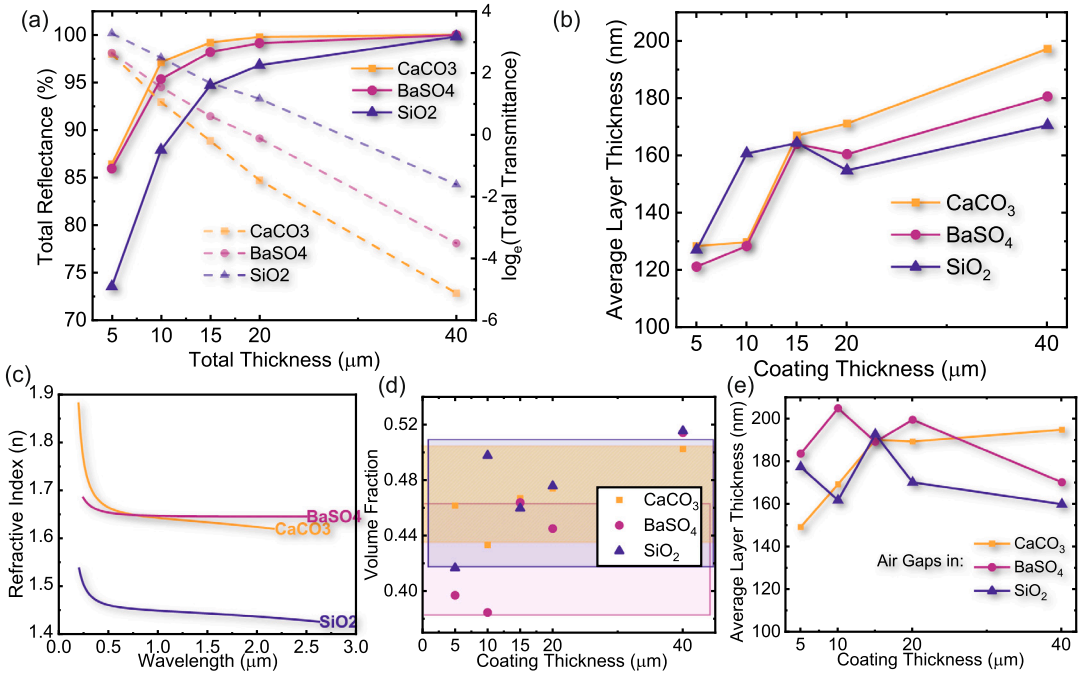

Fig. 5. (a) Comparison of optimized total reflectance and log(Transmittance) for $CaCO_3$, $BaSO_4$ and SiO_2. (b) Increasing trend of average material layer thickness in GA optimized coatings. (c) Wavelength-dependent refractive indices for the materials in consideration. (d) Optimized volume fractions obtained for different coating thicknesses with area spread mapped for each material. (e) Trend of average air gap layer thickness in optimized coatings.

Furthermore, identical to Sec. 3.1, we also perform the optimization using three different objective functions - the R_{solar}, ε_{sky}, and RC for the $BaSO_4$ and SiO_2 multilayers. A higher sky window emissivity is observed in $BaSO_4$ (~0.9) and SiO_2 (~0.5) multilayers due to the presence of resonance peaks in the 8-13 μm wavelength range. The sky window emissivity of $BaSO_4$ is much higher than SiO_2 and $CaCO_3$, which gives it an edge in radiative cooling, this is also demonstrated by Li et al. using their cooling paint [5]. However, the R_{solar} and RC-optimized multilayers still show closely identical behavior, demonstrating the stronger influence of solar reflectivity in radiative cooling. Details of the results can be found in the Table S1 of the SI.

The multilayer optimization performed in this work uses a minimum bit size of 10 nm to increase the optimization precision. By leveraging the ecological phenomenon, this research enables the prediction of a theoretical maximum by incorporating a greater number of layers into the multilayer structure and extract insights from it. The structures can be simplified by compromising the performance through various adjustments like increasing bit size, adding constraints for the number of layers, etc. It will be challenging to manufacture such multilayers, while nanopillar-like structures or other materials like polymers in place of air gaps can be used to provide the desired refractive index contrast.

4. Conclusion

This work investigated a biologically inspired multilayer structure to unlock its maximum potential for ultra-reflective coatings. The proposed design stacks calcium carbonate (reflective material) with air gaps, miming a snell's shell known for surviving in extreme conditions. We use an evolutionary GA to optimize using the R_{solar}, RC and ε_{sky} objective functions. Our results indicate low sky window emissivity in the $CaCO_3$ multilayer which is a biological constraint, while the R_{solar} and RC optimization result in an identical maximum, making R_{solar} the primary focus here. Next, we manually searched for a 20 μm periodic multilayer structure by varying the layer thicknesses. TMM calculations were performed on these structures and maximum total solar reflectance of ~89% was obtained at 170 nm layer thickness. The study showed a distinct correlation between the layer thickness and the peak of spectral reflectance, which prompts the maximum solar reflectance of the periodic multilayer. We optimized this structure to exploit the vast design space of multilayers and obtained a solar reflectance of 99.8% at 20 μm coating thickness. The GA-optimized reflectance was far superior to the manual search. We further optimized and analyzed coatings of 5 μm, 10 μm and 40 μm. The optimized solar reflectance in these multilayers also significantly beats our baseline standard and shows significant cooling power for radiative cooling. The spectral analysis showed that the GA prioritizes reflecting the wavelengths with higher intensity of solar irradiation. It stacks up layers of varying thicknesses such that the incident photons can be localized in the coating. We further validated this understanding by employing the GA on other known solar reflective materials - barium sulfate and silicon dioxide. The average material layer thickness thus obtained follows an increasing trend with increasing coating thickness. GA also finds it more accessible for bigger coatings to localize the longer wavelengths by including larger layers, which results in the increasing trend we have observed. We also established the optimized volume fraction to be ~50% in the multilayer design.

Our analysis helps in understanding the underlying mechanisms of biological and multilayer systems. It will help exploit the multilayer design for enhanced reflectance in bio-inspired design and manufacturing in the future.

CRediT authorship contribution statement

Krutarth Khot: Data curation, Formal analysis, Investigation, Methodology, Writing – original draft, Writing – review & editing. **Prabudhya Roy Chowdhury:** Methodology, Writing – review & editing. **Xiulin Ruan:** Conceptualization, Funding acquisition, Writing – review & editing.

Declaration of competing interest

The authors declare the following financial interests/personal relationships which may be considered as potential competing interests:

Xiulin Ruan reports financial support was provided by National Science Foundation. If there are other authors, they declare that they have

no known competing financial interests or personal relationships that could have appeared to influence the work reported in this paper.

Data availability

Data will be made available on request.

Acknowledgements

K.K. and X.R. acknowledge partial support from the US National Science Foundation through award 2102645.

Appendix A. Supplementary material

Supplementary material related to this article can be found online at https://doi.org/10.1016/j.ijheatmasstransfer.2024.125303.

References

[1] K. Schmidt-Nielsen, C.R. Taylor, A. Shkolnik, Desert snails: problems of heat, water and food, J. Exp. Biol. 55 (1971) 385–398, https://doi.org/10.1242/jeb.55.2.385.
[2] M. Schweizer, R. Triebskorn, H.R. Köhler, Snails in the sun: strategies of terrestrial gastropods to cope with hot and dry conditions, Ecol. Evol. 9 (2019) 12940–12960, https://doi.org/10.1002/ECE3.5607.
[3] S. Parveen, A. Chakraborty, D.K. Chanda, S. Pramanik, A. Barik, G. Aditya, Microstructure analysis and chemical and mechanical characterization of the shells of three freshwater snails, ACS Omega 5 (2020) 25757–25771, https://doi.org/10.1021/acsomega.0c03064, https://pubs.acs.org/doi/10.1021/acsomega.0c03064.
[4] X. Li, J. Peoples, Z. Huang, Z. Zhao, J. Qiu, X. Ruan, Full daytime sub-ambient radiative cooling in commercial-like paints with high figure of merit, Cell Rep. Phys. Sci. 1 (2020) 100221, https://doi.org/10.1016/J.XCRP.2020.100221.
[5] X. Li, J. Peoples, P. Yao, X. Ruan, Ultrawhite baso4paints and films for remarkable daytime subambient radiative cooling, ACS Appl. Mater. Interfaces 13 (2021) 21733–21739, https://doi.org/10.1021/acsami.1c02368.
[6] J. Peoples, X. Li, Y. Lv, J. Qiu, Z. Huang, X. Ruan, A strategy of hierarchical particle sizes in nanoparticle composite for enhancing solar reflection, https://doi.org/10.1016/j.ijheatmasstransfer.2018.11.059, 2019.
[7] W. Gellermann, M. Kohmoto, B. Sutherland, P.C. Taylor, Localization of light waves in Fibonacci dielectric multilayers, Phys. Rev. Lett. 72 (1994) 633, https://doi.org/10.1103/PhysRevLett.72.633, https://journals.aps.org/prl/abstract/10.1103/PhysRevLett.72.633.
[8] E. Yablonovitch, Engineered omnidirectional external-reflectivity spectra from one-dimensional layered interference filters, https://doi.org/10.1364/ol.23.001648, 1998.
[9] J.N. Winn, Y. Fink, S. Fan, J.D. Joannopoulos, Omnidirectional reflection from a one-dimensional photonic crystal, 1998.
[10] X.L. Ruan, M. Kaviany, Photon localization and electromagnetic field enhancement in laser-irradiated, random porous media, Microscale Thermophys. Eng. 9 (2005) 63–84, https://doi.org/10.1080/10893950590913404.
[11] J.D. Joannopoulos, S.G. Johnson, J.N. Winn, R.D. Meade, Photonic Crystals: Molding the Flow of Light, Princeton University Press, 2011.
[12] Y. Huang, M. Pu, Z. Zhao, X. Li, X. Ma, X. Luo, Broadband metamaterial as an “invisible” radiative cooling coat, Opt. Commun. 407 (2018) 204–207, https://doi.org/10.1016/j.optcom.2017.09.036.
[13] H. Wei, H. Bao, X. Ruan, Genetic algorithm-driven discovery of unexpected thermal conductivity enhancement by disorder, Nano Energy 71 (2020) 104619, https://doi.org/10.1016/J.NANOEN.2020.104619.
[14] P.R. Chowdhury, X. Ruan, Unexpected thermal conductivity enhancement in aperiodic superlattices discovered using active machine learning, npj Comput. Mater. 8 (2022) 1–7, https://doi.org/10.1038/s41524-022-00701-1, https://www.nature.com/articles/s41524-022-00701-1, 2022.
[15] M.F. Schubert, F.W. Mont, S. Chhajed, D.J. Poxson, J.K. Kim, E.F. Schubert, Design of multilayer antireflection coatings made from co-sputtered and low-refractive-index materials by genetic algorithm, 2008.
[16] M. Zeyghami, E. Stefanakos, D.Y. Goswami, Development of one-dimensional photonic selective emitters for energy harvesting applications, Sol. Energy Mater. Sol. Cells 163 (2017) 191–199, https://doi.org/10.1016/J.SOLMAT.2017.01.026.
[17] W. Zhang, B. Wang, C. Zhao, Selective thermophotovoltaic emitter with aperiodic multilayer structures designed by machine learning, ACS Appl. Energy Mater. 4 (2021) 2004–2013, https://doi.org/10.1021/ACSAEM.0C03201, https://pubs.acs.org/doi/full/10.1021/acsaem.0c03201.
[18] D. Chae, M. Kim, P.H. Jung, S. Son, J. Seo, Y. Liu, B.J. Lee, H. Lee, Spectrally selective inorganic-based multilayer emitter for daytime radiative cooling, ACS Appl. Mater. Interfaces 12 (2020) 8073–8081, https://doi.org/10.1021/acsami.9b16742.
[19] Y. Zhu, Y.H. Ye, D. Wang, Y. Cao, Quasi-periodic selective multilayer emitter for sub-ambient daytime radiative cooling, AIP Adv. 11 (2021) 025109, https://doi.org/10.1063/5.0035138, https://aip.scitation.org/doi/abs/10.1063/5.0035138.
[20] P. You, X. Li, Y. Huang, X. Ma, M. Pu, Y. Guo, X. Luo, High-performance multilayer radiative cooling films designed with flexible hybrid optimization strategy, Materials 13 (2020), https://doi.org/10.3390/MA13132885.
[21] M. Kim, J. Seo, S. Yoon, H. Lee, J. Lee, B.J. Lee, Optimization and performance analysis of a multilayer structure for daytime radiative cooling, J. Quant. Spectrosc. Radiat. Transf. 260 (2021), https://doi.org/10.1016/J.JQSRT.2020.107475.
[22] G. Mabchour, M. Benlattar, K. Saadouni, M. Mazroui, Daytime radiative cooling purposes with selective multilayer design based on ta2o5, Optik 214 (2020) 164811, https://doi.org/10.1016/J.IJLEO.2020.164811.
[23] S. Kim, W. Shang, S. Moon, T. Pastega, E. Lee, T. Luo, High-performance transparent radiative cooler designed by quantum computing, ACS Energy Lett. 7 (2022) 4134–4141, https://doi.org/10.1021/acsenergylett.2c01969.
[24] A. Sakurai, K. Yada, T. Simomura, S. Ju, M. Kashiwagi, H. Okada, T. Nagao, K. Tsuda, J. Shiomi, Ultranarrow-band wavelength-selective thermal emission with aperiodic multilayered metamaterials designed by bayesian optimization, http://pubs.acs.org/journal/acscii, 2019, https://doi.org/10.1021/acscentsci.8b00802.
[25] Y. Shi, W. Li, A. Raman, S. Fan, Optimization of multilayer optical films with a memetic algorithm and mixed integer programming, ACS Photonics 5 (2018) 684–691, https://doi.org/10.1021/acsphotonics.7b01136.
[26] Z.F. Mira, S.-Y. Heo, D.H. Kim, G.J. Lee, Y.M. Song, Multilayer selective passive daytime radiative cooler optimization utilizing memetic algorithm, J. Quant. Spectrosc. Radiat. Transf. 272 (2021) 107774, https://doi.org/10.1016/j.jqsrt.2021.107774, https://www.sciencedirect.com/science/article/pii/S0022407321002673.
[27] A.V. Tikhonravov, G.W. DeBell, M.K. Trubetskov, Application of the needle optimization technique to the design of optical coatings, Appl. Opt. 35 (28) (1996) 5493–5508, https://doi.org/10.1364/AO.35.005493.
[28] L. Zeng, Y. Yi, C. Hong, J. Liu, N. Feng, X. Duan, L.C. Kimerling, B.A. Alamariu, Efficiency enhancement in si solar cells by textured photonic crystal back reflector, Appl. Phys. Lett. 89 (2006) 111111, https://doi.org/10.1063/1.2349845, https://aip.scitation.org/doi/abs/10.1063/1.2349845.
[29] D. Zhou, R. Biswas, Photonic crystal enhanced light-trapping in thin film solar cells, J. Appl. Phys. 103 (2008), https://doi.org/10.1063/1.2908212.
[30] A. Chutinan, N.P. Kherani, S. Zukotynski, K.A. Münzer, K.T. Holdermann, R.E. Schlosser, S. Sterk, L. Zeng, Y. Yi, C. y Hong, J. Liu, N. Feng, X. Duan, L.C. Kimerling, B. Alamariu, High-efficiency photonic crystal solar cell architecture, Opt. Express 17 (11) (2009) 8871–8878, https://doi.org/10.1364/OE.17.008871.
[31] A. Abbasiyan, M. Noori, H. Baghban, Efficiency enhancement in si solar cell using 1d quasi-periodic antireflection coating, Opt. Quantum Electron. 51 (2019) 1–10, https://doi.org/10.1007/S11082-019-2056-9/FIGURES/8, https://link.springer.com/article/10.1007/s11082-019-2056-9.
[32] P. Roy Chowdhury, K. Khot, J. Song, Z. He, D. Kortge, Z. Han, P. Bermel, H. Wang, X. Ruan, Machine learning designed and experimentally confirmed enhanced reflectance in aperiodic multilayer structures, Adv. Opt. Mater. 2300610 (2023), https://doi.org/10.1002/adom.202300610.
[33] K. Yao, H. Ma, M. Huang, H. Zhao, J. Zhao, Y. Li, S. Dou, Y. Zhan, Near-perfect selective photonic crystal emitter with nanoscale layers for daytime radiative cooling, ACS Appl. Nano Mater. 2 (2019) 5512–5519, https://doi.org/10.1021/acsanm.9b01097.
[34] B.B. Naghshine, A. Saboonchi, Optimized thin film coatings for passive radiative cooling applications, Opt. Commun. 410 (2018) 416–423, https://doi.org/10.1016/j.optcom.2017.10.047.
[35] B. Ko, D. Lee, T. Badloe, J. Rho, Metamaterial-based radiative cooling: towards energy-free all-day cooling, https://doi.org/10.3390/en12010089, 2019.
[36] K. Yu, L. Li, K. Shi, H. Liu, Y. Hu, K. Zhang, Y. Liu, X. Wu, Near-field radiative heat transfer between multilayer structures composed of different hyperbolic materials, Int. J. Heat Mass Transf. 211 (2023) 124229, https://doi.org/10.1016/j.ijheatmasstransfer.2023.124229, https://www.sciencedirect.com/science/article/pii/S0017931023003812.
[37] X. Liu, R. Zhang, Z. Zhang, Near-field radiative heat transfer with doped-silicon nanostructured metamaterials, Int. J. Heat Mass Transf. 73 (2014) 389–398, https://doi.org/10.1016/j.ijheatmasstransfer.2014.02.021, https://www.sciencedirect.com/science/article/pii/S0017931014001380.
[38] S. Mukhopadhyay, C.T. Ellis, D.C. Ratchford, E.M. Jackson, J.G. Tischler, T.L. Reinecke, M.D. Johannes, Natural hyperbolicity in bulk calcite, J. Appl. Phys. 130 (2021) 143101, https://doi.org/10.1063/5.0064946.
[39] G. Ghosh, Dispersion-equation coefficients for the refractive index and birefringence of calcite and quartz crystals, Opt. Commun. 163 (1999) 95–102, https://doi.org/10.1016/S0030-4018(99)00091-7.
[40] I.H. Malitson, Interspecimen comparison of the refractive index of fused silica, J. Opt. Soc. Am. 55 (10) (1965) 1205–1209, https://doi.org/10.1364/JOSA.55.001205.
[41] C.Z. Tan, Determination of refractive index of silica glass for infrared wavelengths by ir spectroscopy, J. Non-Cryst. Solids 223 (1998) 158–163, https://doi.org/10.1016/S0022-3093(97)00438-9.
[42] Z. Tong, J. Peoples, X. Li, X. Yang, H. Bao, X. Ruan, Electronic and phononic origins of baso4 as an ultra-efficient radiative cooling paint pigment, Mater. Today Phys. 24 (2022) 100658, https://doi.org/10.1016/j.mtphys.2022.100658, https://www.sciencedirect.com/science/article/pii/S2542529322000566.
[43] C.C. Katsidis, D.I. Siapkas, General transfer-matrix method for optical multilayer systems with coherent, partially coherent, and incoherent interference, Appl. Opt. 41 (19) (2002) 3978–3987, https://doi.org/10.1364/AO.41.003978.

[44] Z. Knittl, Optics of Thin Films: An Optical Multilayer Theory, Wiley Series in Pure and Applied Optics, Wiley, New York, 1976.
[45] ASTM, Standard tables for reference solar spectral irradiances: direct normal and hemispherical on 37° tilted surface, https://www.astm.org/g0173-03r12.html, 2012, https://doi.org/10.1520/G0173-03R12.
[46] X. Sun, Y. Sun, Z. Zhou, M.A. Alam, P. Bermel, Radiative sky cooling: fundamental physics, materials, structures, and applications, Nanophotonics 6 (2017) 997–1015, https://doi.org/10.1515/NANOPH-2017-0020/ASSET/GRAPHIC/J_NANOPH-2017-0020_FIG_013.JPG, https://www.degruyter.com/document/doi/10.1515/nanoph-2017-0020/html?lang=en.
[47] A. Felicelli, I. Katsamba, F. Barrios, Y. Zhang, Z. Guo, J. Peoples, G. Chiu, X. Ruan, Thin layer lightweight and ultrawhite hexagonal boron nitride nanoporous paints for daytime radiative cooling, Cell Rep. Phys. Sci. 3 (2022) 101058, https://doi.org/10.1016/j.xcrp.2022.101058, https://www.sciencedirect.com/science/article/pii/S2666386422003526.
[48] Z. Huang, X. Ruan, Nanoparticle embedded double-layer coating for daytime radiative cooling, Int. J. Heat Mass Transf. 104 (2017) 890–896, https://doi.org/10.1016/j.ijheatmasstransfer.2016.08.009.
[49] D.J. Murray-Smith, Experimental modelling: system identification, parameter estimation and model optimisation techniques, in: Modelling and Simulation of Integrated Systems in Engineering, 2012, pp. 165–214.
[50] S. Jena, R.B. Tokas, P. Sarkar, J.S. Misal, S.M. Haque, K.D. Rao, S. Thakur, N.K. Sahoo, Omnidirectional photonic band gap in magnetron sputtered tio2/sio2 one dimensional photonic crystal, Thin Solid Films 599 (2016) 138–144, https://doi.org/10.1016/J.TSF.2015.12.069.